THE ASTRONOMICAL JOURNAL, 120:2496–2512, 2000 November

MAPPING THE GALACTIC HALO. II. PHOTOMETRIC SURVEY

R. C. DOHM-PALMER
Department of Astronomy, University of Michigan, Ann Arbor, MI 48109; Steward Observatory, University of Arizona, Tucson, AZ 85721; rdpalmer@astro.lsa.umich.edu

MARIO MATEO
Department of Astronomy, University of Michigan, Ann Arbor, MI 48109; mateo@astro.lsa.umich.edu

E. OLSZEWSKI
Steward Observatory, University of Arizona, Tucson, AZ 85721; edo@as.arizona.edu

H. MORRISON[1]
Department of Astronomy and Department of Physics, Case Western Reserve University, Cleveland, OH 44106; heather@vegemite.astr.cwru.edu

PAUL HARDING
Steward Observatory, University of Arizona, Tucson, AZ 85721; and Department of Astronomy, Case Western Reserve University, Cleveland, OH 44106; harding@billabong.astr.cwru.edu

AND

KENNETH C. FREEMAN AND JOHN NORRIS
Mount Stromlo and Siding Spring Observatories ANU, Private Bag, Weston Creek, 2611 Canberra, ACT Australia; kcf@mso.anu.edu.au, jen@mso.anu.edu.au
Received 2000 July 11; accepted 2000 July 31

ABSTRACT

We present imaging results from a high Galactic latitude survey designed to examine the structure of the Galactic halo. The objective of the survey is to identify candidate halo stars which can be observed spectroscopically to obtain radial velocities and confirm halo membership. The Washington filter system is used for its ability to distinguish between dwarfs and giants, as well as provide a metallicity indicator. Our most successful imaging run used the BTC camera on the CTIO 4 m telescope in 1999 April. Photometric conditions during these observations provided superb photometry, with average errors for a star at $M = 18.5$ of 0.009, 0.008, 0.011, and 0.009 for C, M, DDO51, and T_2, respectively. We use these data as a template to describe the details of our photometric reduction process. It is designed to perform CCD reductions and stellar photometry automatically during the observation run, without the aid of external packages, such as IRAF and IDL. We describe necessary deviations from this procedure for other instruments used in the survey up to 2000 June. Preliminary results from spectroscopic observations indicate a 97% efficiency in eliminating normal dwarfs from halo giant candidates for $M < 18.5$. Unfortunately, low-metallicity subdwarfs cannot be photometrically distinguished from giants using the Washington filters. These major contaminants unavoidably reduced the overall giant identification efficiency to 66% for $M < 18.5$. Our improved knowledge of these stars will increase this efficiency for future spectroscopic observations.

Key words: Galaxy: evolution — Galaxy: formation — Galaxy: halo — Galaxy: stellar content

1. INTRODUCTION

A revolution is underway in our understanding of how galaxies form. The idea of a monolithic collapse of a single system at earliest times (Eggen, Lynden-Bell, & Sandage 1962) has been challenged by observations at high redshift and by increasingly sophisticated models of the evolution of structures within the basic framework of the hot big bang model (Steinmetz & Mueller 1994). These findings imply that we should see clear evidence of hierarchical formation processes within nearby galaxies. Indeed, some of the earliest work that suggested complex and possibly hierarchical evolutionary histories for galaxies such as ours came from studies of the stellar populations of the outer halo of the Milky Way (Searle & Zinn 1978). Studies of nearby and high-redshift systems represent complementary approaches. No viable model of galaxy formation can be considered successful unless the evidence from both sources can be understood within a single framework.

The fossil record of the local galaxian population remains sparsely sampled. The halo is the most likely component to retain information of the Galaxy's formation history. Apart from the isolated (and possibly peculiar) star clusters and dwarf galaxies, much of our knowledge of the halo derives from a relatively small number of nearby stars "passing through" the solar neighborhood. Surveys that extend a few kiloparsecs from the Sun isolate halo stars more effectively, but even so, contamination by thick disk stars and background galaxies can be significant. The remoteness of the Magellanic Clouds and M31 make direct efforts to identify substructure in their halos extremely challenging.

Despite the difficulties, recent studies of our Galaxy have begun to reveal tantalizing evidence of possible substructure in the halo (Majewski 1992; Côté et al. 1993; Arnold & Gilmore 1992; Helmi et al. 1999; Yanny, Newberg, & Kent 2000). More spectacularly, the discovery of the SGR dwarf galaxy (Ibata, Gilmore, & Irwin 1994) provides indisputable

[1] Cottrell Scholar of Research Corporation and NSF CAREER fellow.

evidence that our Galaxy's halo is accreting stars and clusters that formed and evolved in an independent galaxy. The question has now shifted from, did accretion play any role in the formation of the Galaxy? to how much of the Galaxy formed from accretion of hierarchical fragments?

This paper continues a series that describes our efforts to address this second question by identifying substructure directly within the Galactic halo. An overview of this survey was presented in Morrison et al. (2000a, hereafter Paper I). To summarize, we are carrying out a large-scale study of high-latitude fields optimized to identify distant halo stars as potential tracers of substructure in the outer Galaxy. Our observational approach is sensitive to a variety of halo stellar inhabitants, including (1) distant halo blue horizontal-branch stars, (2) blue metal-poor stars (BMP; Preston, Beers, Shectman 1994) (observationally, these are field analogs of blue stragglers found in star clusters; Bailyn 1995), (3) halo turnoff stars, and (4) red giants. The bluer stars can be identified photometrically with relative ease using any number of combinations of broadband colors. The Sloan Digital Sky Survey (Yanny et al. 2000) and our survey (Paper I) have already proven very effective at doing so. These can be considered wide-field extensions of the surveys of Hawkins (Norris & Hawkins 1991).

Identification of the red giants, however, demands more precise and specialized photometric observations and added care to identify and remove contaminants. But this effort does have important rewards: red giants are the most luminous tracers found in significant numbers in the halo and hence allow us to probe to the greatest depth. Conceivably, luminous giants can be identified at distances as large as 200 kpc in our survey, though the giant-branch luminosity function ensures that the bulk of the stars we find will be between 20–100 kpc distant. Certain important biases that are inherent in the studies of horizontal-branch stars (Kinman et al. 1994) are also avoided by isolating red giants, whose properties are well understood as a function of age and metallicity. In addition, studies of the chemical evolution of the outer halo will be possible via detailed abundance analysis of halo giants using 10 m–class telescopes. These studies are much more difficult for the hotter horizontal-branch stars.

The purpose of this paper is twofold: to describe the procedures we have developed to carry out the photometric observations of our survey and to publish the photometry of photometrically calibrated fields. Our approach employs the modified Washington photometric system (Canterna 1976; Geisler 1984) to provide indices that can be used to isolate the four classes of stars described above. We use four filters in our survey to produce indices sensitive to temperature ($M-T_2$), surface gravity/luminosity ($M-51$), and metallicity ($C-M$). These indices provide the means of selecting halo giants from the blanket of thin and thick disk stars and unresolved galaxies, the sum of which dominate the point sources in any halo field. It should be noted that the luminosity discrimination of the 51 filter is based on the strength of Mg hydride band and Mg b lines. Thus, at low metallicities the ability to photometrically distinguish subdwarfs from giants disappears (Morrison et al. 2000b).

Our observational procedures were first developed for use at the Burrell Schmidt[2] and CTIO Schmidt telescopes. The basic approach was subsequently carried over to the NOAO 4 m telescopes, where our survey efficiency is much higher. The first of these runs employed the BTC camera on the CTIO 4 m telescope in 1999 April; it has proven to be the most successful run to date.

A subset of photometric red giant and horizontal branch candidates produced from these data sets have been observed spectroscopically. These observations provide a test for our photometric selection techniques and will be briefly discussed here. More details on the spectroscopy can be found in Paper I and in future papers of this series. Two important conclusions from these spectroscopic observations are worth stating here.

First, selection of distant red giants *demands* high-quality photometry, not only to define the luminosity index ($M-51$), but also to minimize contamination from the many stellar and galaxian contaminants found in all fields. When foreground dwarfs outnumber the rare giants by orders of magnitude, even 3 or 4 σ errors can produce red-giant imposters. Our photometric procedures represent a balance between the need for precise photometric indices and the need for an efficient deep survey of a significant fraction of the halo. Second, even with perfect photometric observations and a highly restrictive set of selection criteria, a photometric sample of distant red giants will be contaminated by metal-poor subdwarfs within the halo. Spectroscopic confirmation is necessary to identify and remove these relatively nearby stars from any deep-halo survey such as ours (Morrison et al. 2000b).

The price of an efficient survey employing mosaics of CCD cameras is a very high data rate; on good nights we obtain 10–15 Gbytes of raw imaging data with the NOAO Mosaic imagers. These data must be reduced quickly to avoid serious backlogs and, more importantly, to promptly identify halo candidates that can be subsequently observed spectroscopically. Our imaging and spectroscopic observations are often scheduled within a few weeks of each other to be able to survey the same high-latitude regions in a given season. Throughout this survey—which has seen an increase in the data rate by a factor of more than 50 in 1.5 years—we have aimed to carry out the full processing and photometric reductions of our imaging data in near real time at the telescope. We have developed software that makes it possible to achieve this goal without using any additional programs or packages such as IRAF or IDL and the associated overhead and costs. This process is robust and flexible enough to handle the inevitable problem images within a large data set.

The following section summarizes the observations and describes the fields that have been observed as of 2000 June. Section 3 describes the automated pipeline for processing images and measuring photometry and, ultimately, astrometry of sufficient precision to support single-slit or multi-object spectroscopy. Section 4 presents the photometric results, emphasizing the precision that we achieve and the efficiency of our photometric selection procedure.

2. OBSERVATION SUMMARY

2.1. *Field Selection*

The goal of this survey is to identify distant halo stars. It is advantageous to avoid the confusion of fields near the Galactic plane, where the fraction of halo stars is extremely

[2] Observations were made with the Burrell Schmidt of the Warner and Swassey Observatory, Case Western Reserve University.

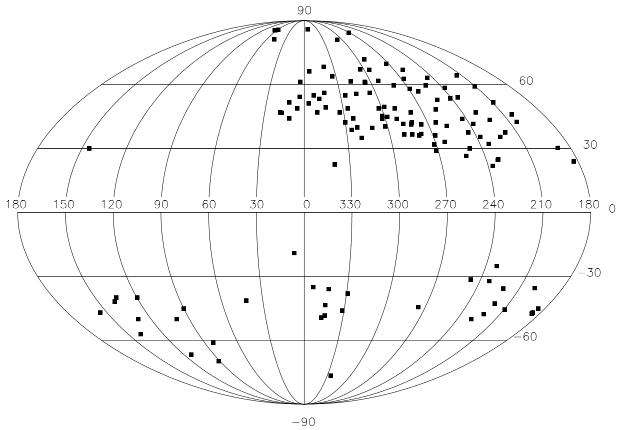

FIG. 1.—Locations of the 134 fields in Galactic longitude and latitude

small. Thus, with a few exceptions, all fields were chosen to have a Galactic latitude of $|b| \gtrsim 25$.

Furthermore, we wish to avoid highly reddened areas to avoid the possibility of differential reddening across a field and to prevent distant halo stars being extincted below detection limits. All potential fields are checked on the reddening maps of Schlegel, Finkbeiner, & Davis (1998). Fields with high extinction or spatially varying reddening are removed. With one exception, all fields have $E(B-V) < 0.13$.

Finally, we wish to avoid placing very bright stars in the images. These will saturate the surrounding region of the CCD chip and add diffraction spikes that can confuse photometric reductions. Depending on how bright such a star is, this saturation can also remove up to 10% or more of a single CCD from the survey area. The Ohio State overlays of the POSS survey were used to choose fields with no stars as bright as SAO stars (Dixon 1981).

Thus far we have imaged 134 fields covering a total area of 52 deg^2. These fields are listed in Table 1. Figures 1 and 2 show the location of these fields in both Galactic and equatorial coordinates.

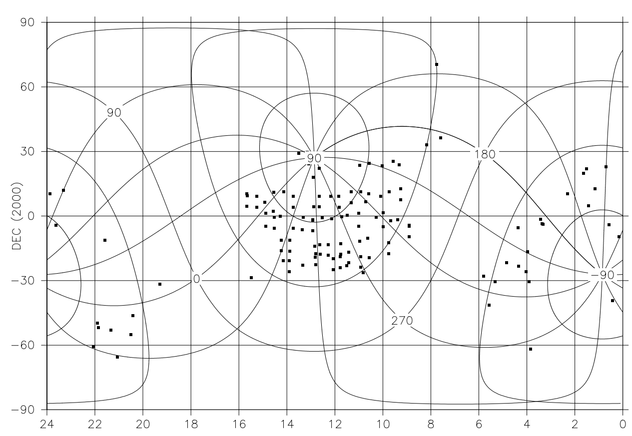

FIG. 2.—Location of the 134 fields in equatorial coordinates. Also plotted is a grid of Galactic coordinates in 30° increments.

2.2. *Instrumentation and Observing Strategy*

As of 2000 June, we have had six observing runs since 1998 October. The observations were taken with four different instruments and three different telescopes. The instruments are as follows: the Burrell Schmidt on KPNO, which used a single SITe 2048 × 4096 CCD with a pixel scale of 1".45 pixel^{-1} and a total area of 1.4 deg^2 per field; the BTC camera on the CTIO 4 m telescope, which consisted of four 2048 × 2048 CCDs with 0".43 pixel^{-1} and a total area of 0.24 deg^2 per field; the first NOAO Mosaic camera, used on the KPNO 4 m with 0".27 pixel^{-1} and a total area of 0.38 deg^2 per field; the second NOAO Mosaic camera used on the CTIO 4 m with 0".25 pixel^{-1} and a total area of 0.38 deg^2 per field.

The most successful observing run was in 1999 April with the BTC camera in which we imaged 53 fields. These data proved to be of excellent quality. This is essential for distinguishing halo candidates from foreground dwarfs. As discussed in § 4, we were highly successful in identifying halo giants from these data.

All four nights in 1999 April were judged photometric through the entire night, so these fields are fully calibrated. All other observing runs had weather-related difficulties for at least part of the run and are only partially calibrated. In subsequent sections we describe the 1999 April reduction procedures as a template for the general reduction procedures used for this survey. Along the way we describe necessary differences specific to each of the other instruments.

Each field's observation consists of a single exposure in each of four filters: C, M, T_2, and DDO51 (Canterna 1976; Geisler 1984). The respective exposure times for each filter were typically 100, 500, 120, and 250 s. With limited success we tried to adjust the exposure times to match the variations in seeing so that every image would have the same photometric sensitivity. The exposure times and observing conditions for each field are listed in Table 2. With only one exception, the air mass of each exposure is <1.8, and most exposures were taken with an air mass <1.5. The seeing ranged from 0".7 to 3".3.

The exceptions to this observing strategy are the eight fields observed with the Burrell Schmidt. Because it is not possible to achieve the necessary photometric depth in a single exposure with this instrument, each field was observed at least four times under good conditions. Each exposure was 1200 s in each filter. We do not list the air-mass and seeing measurements for individual exposures. Poor images are removed, and photometry from the remaining images is averaged prior to being calibrated (see § 3.4 for a full discussion).

For the 4 m runs, focus offsets for each filter were determined at the beginning of the run. The telescope was then focused in a single filter at the beginning of each night and during the night if necessary. The focus was adjusted, using the standard formula for the 4 m telescopes, as the temperature changed throughout the night. Focus for the Schmidt observations was adjusted throughout the night as required.

There is one logistic oddity concerning the BTC chip numbers. The chip numbers referred to in this paper are not the conventional numbers for the BTC camera. It was determined that chips 1 and 2 had been exchanged in the readout electronics accidentally during instrument setup.

TABLE 1

OBSERVED FIELDS

Name	l	b	R.A.[a]	Decl.[a]	$E(B-V)$	Date[b]	Instrument[c]	Conditions[d]
l0034bp541	3.4	54.1	14 55 00.45	6 26 18.2	0.034	2000 Apr 8	Mosaic-S	
l0037bp613	3.7	61.3	14 32 32.00	11 01 32.5	0.024	1999 Apr 8	BTC	
l0055bp488	5.5	48.8	15 14 59.15	4 11 14.6	0.041	2000 Apr 9	Mosaic-S	
l0064bm190......	6.4	−19.0	19 17 38.74	−31 37 27.9	0.110	2000 Apr 10	Mosaic-S	Clouds
l0111bp440	11.1	44.0	15 39 39.07	4 30 43.9	0.056	2000 Apr 8	Mosaic-S	
l0118bp517	11.8	51.7	15 14 48.25	9:08 53.0	0.032	1999 Apr 7	BTC	
l0171bp467	17.1	46.7	15 39 24.00	9:30 59.9	0.035	1999 Apr 8	BTC	
l0182bp470	18.2	47.0	15 39 50.17	10 19 09.8	0.047	2000 Apr 8	Mosaic-S	
l0420bm414......	42.0	−41.4	21 35 10.95	−11 19 20.8	0.044	1999 Oct 31	Mosiac-S	Clouds
l0481bp813	48.1	81.3	13 29 54.05	29 04 31.7	0.010	2000 Feb 14	Mosaic-N	Clouds
l0592bp857	59.2	85.7	13 09 03.99	28 57 44.2	0.010	2000 Feb 14	Mosaic-N	Clouds
l0645bp855	64.5	85.5	13 09 02.55	29 24 54.6	0.011	2000 Feb 14	Mosaic-N	Clouds
l0658bp855	65.8	85.5	13 08 48.43	29 30 12.1	0.011	2000 Feb 14	Mosaic-N	Clouds
l0820bm610......	82.0	−61.0	23 37 09.27	−4 10 37.4	0.036	1999 Oct 31	Mosiac-S	Clouds
l0900bm450......	90.0	−45.0	23 18 55.03	11 52 27.7	0.043	1998 Oct-Nov	B. Schmidt	Clouds
l0915bm698......	91.5	−69.8	0 09 21.24	−9 32 21.0	0.036	1999 Oct 31	Mosiac-S	Clouds
l1000bm500......	100.0	−50.0	23 52 27.72	10 13 39.0	0.124	1998 Oct	B. Schmidt	Clouds
l1124bm666......	112.4	−66.6	0 34 44.62	−4 04 12.9	0.033	1999 Oct 31	Mosiac-S	Clouds
l1200bm400......	120.0	−40.0	0 41 41.52	22 48 58.4	0.034	1998 Nov	B. Schmidt	Clouds
l1300bm500......	130.0	−50.0	1 10 01.99	12 36 58.8	0.041	1998 Oct	B. Schmidt	Clouds
l1350bm400......	135.0	−40.0	1 31 12.47	21 56 16.6	0.065	1998 Oct	B. Schmidt	Clouds
l1379bm417......	137.9	−41.7	1 38 44.61	19 47 33.7	0.046	1999 Oct 30	Mosiac-S	
l1390bm570......	139.0	−57.0	1 26 14.38	4 46 55.3	0.022	1999 Oct 31	Mosiac-S	Clouds
l1450bp300	145.0	30.0	7 46 02.80	70 26 15.4	0.028	1998 Nov	B. Schmidt	Clouds
l1550bm470......	155.0	−47.0	2 17 50.81	10 25 13.9	0.066	1998 Nov	B. Schmidt	Clouds
l1828bp240	182.8	24.0	7 35 14.49	36 24 48.4	0.048	2000 Feb 14	Mosaic-N	Clouds
l1850bm450......	185.0	−45.0	3 26 09.45	−1 35 02.7	0.068	1998 Oct	B. Schmidt	Clouds
l1861bm475......	186.1	−47.5	3 20 06.00	−3 42 53.3	0.037	1999 Oct 30	Mosiac-S	
l1862bm470......	186.2	−47.0	3 21 51.60	−3 27 58.5	0.030	1999 Oct 31	Mosiac-S	Clouds
l1886bp302	188.6	30.2	8 11 05.83	33 06 47.3	0.046	2000 Feb 14	Mosaic-N	Clouds
l1994bm354......	199.4	−35.4	4 22 27.42	−5 24 59.6	0.045	1999 Oct 31	Mosiac-S	Clouds
l2035bp460	203.5	46.0	9 34 01.23	25 25 28.3	0.020	2000 Feb 14	Mosaic-N	Clouds
l2045bp424	204.5	42.4	9 19 29.78	23 49 06.8	0.034	2000 Feb 14	Mosaic-N	Clouds
l2090bp517	209.0	51.7	10 02 09.58	23 18 27.8	0.033	2000 Feb 14	Mosaic-N	Clouds
l2092bm457......	209.2	−45.7	3 58 04.54	−16 36 42.7	0.029	1999 Oct 30	Mosiac-S	
l2102bp592	210.2	59.2	10 34 44.55	24 25 05.3	0.019	2000 Feb 14	Mosaic-N	Clouds
l2144bp643	214.4	64.3	10 58 27.66	23 38 24.1	0.018	2000 Feb 14	Mosaic-N	Clouds
l2179bp376	217.9	37.6	9 15 35.80	12 32 30.5	0.025	1999 Apr 9	BTC	
l2203bm428......	220.3	−42.8	4 20 45.58	−23 10 34.0	0.031	1999 Nov 1	Mosiac-S	
l2211bm357......	221.1	−35.7	4 50 52.50	−21 38 23.5	0.045	1999 Nov 1	Mosiac-S	
l2223bm477......	222.3	−47.7	4 01 28.13	−25 46 11.8	0.028	1999 Nov 1	Mosiac-S	
l2233bp433	223.3	43.3	9 43 52.04	11 18 43.6	0.019	1999 Apr 9	BTC	
l2235bp354	223.5	35.4	9 15 43.54	7 31 57.8	0.054	2000 Apr 9	Mosaic-S	Clouds
l2291bm501......	229.1	−50.1	3 54 12.93	−30 34 57.6	0.011	1999 Oct 30	Mosiac-S	
l2297bp469	229.7	46.9	10 05 28.62	9 03 43.6	0.032	1999 Apr 8	BTC	
l2321bp249	232.1	24.9	8 54 35.73	−4 11 25.2	0.017	1999 Oct 30	Mosiac-S	
l2326bp246	232.6	24.6	8 54 33.91	−4 44 04.2	0.017	1999 Apr 10	BTC	
l2328bm252......	232.8	−25.2	5 48 45.40	−27 53 36.5	0.031	1999 Nov 1	Mosiac-S	
l2336bm321......	233.6	−32.1	5 19 23.86	−30 13 29.0	0.016	1999 Oct 30	Mosiac-S	
l2341bp321	234.1	32.1	9 22 34.61	−1 42 56.0	0.032	1999 Apr 9	BTC	
l2342bp539	234.2	53.9	10 35 45.99	10 15 58.4	0.029	1999 Apr 9	BTC	
l2371bp218	237.1	21.8	8 54 24.75	−9 43 42.3	0.036	2000 Apr 8	Mosaic-S	
l2373bp416	237.3	41.6	9 59 36.56	1 36 45.8	0.019	1999 Apr 10	BTC	
l2376bp354	237.6	35.4	9 40 04.23	−2 12 50.6	0.027	1999 Apr 9	BTC	
l2376bp585	237.6	58.5	10 55 37.70	11 13 40.1	0.018	1999 Apr 8	BTC	
l2410bp534	241.0	53.4	10 43 29.75	6 41 03.5	0.034	2000 Apr 8	Mosaic-S	
l2432bp438	243.2	43.8	10 17 10.88	−0 28 05.6	0.046	1999 04/10	BTC	
l2441bp375	244.1	37.5	9 59 36.18	−5 02 22.4	0.029	2000 Apr 8	Mosaic-S	
l2449bp632	244.9	63.2	11 19 37.91	11 13 06.6	0.023	1999 Apr 9	BTC	
l2468bm314......	246.8	−31.4	5 34 38.39	−41 22 10.0	0.024	1999 Oct 30	Mosiac-S	
l2481bp300	248.1	30.0	9 45 32.65	−12 28 15.1	0.036	1999 Apr 10	BTC	
l2522bp266	252.2	26.6	9 45 22.56	−17 25 43.9	0.062	2000 Apr 9	Mosaic-S	Clouds
l2524bp528	252.4	52.8	11 00 07.15	1 12 47.3	0.034	1999 Apr 10	BTC	
l2525bp597	252.5	59.7	11 19 19.26	6 10 51.5	0.077	2000 Apr 8	Mosaic-S	
l2574bp405	257.4	40.5	10 37 34.16	−10 14 58.1	0.039	1999 Apr 9	BTC	

TABLE 1—*Continued*

Name	l	b	R.A.[a]	Decl.[a]	$E(B-V)$	Date[b]	Instrument[c]	Conditions[d]
l2586bp483	258.6	48.3	11 00 12.74	−4 45 47.5	0.035	2000 Apr 10	Mosaic-S	Clouds
l2611bp668	261.1	66.8	11 49 42.83	9 05 00.9	0.024	1999 Apr 9	BTC	
l2634bp567	263.4	56.7	11 29 37.20	0 14 37.5	0.023	1999 Apr 9	BTC	
l2637bp330	263.7	33.0	10 34 41.87	−19 15 26.9	0.055	1999 Apr 8	BTC	
l2638bp423	263.8	42.3	10 57 32.06	−11 45 18.1	0.033	1999 Apr 8	BTC	
l2676bp626	267.6	62.6	11 49 32.40	4 03 14.0	0.026	2000 Apr 8	Mosaic-S	
l2682bp361	268.2	36.1	10 55 02.89	−18 48 10.1	0.037	1999 Apr 10	BTC	
l2690bp580	269.0	58.0	11 42 36.80	−0 15 50.6	0.025	1999 Apr 10	BTC	
l2713bp319	271.3	31.9	10 55 01.87	−23 43 33.5	0.070	2000 Apr 10	Mosaic-S	Clouds
l2715bp289	271.5	28.9	10 48 52.59	−26 23 17.6	0.089	2000 Apr 9	Mosaic-S	Clouds
l2717bp842	271.7	84.2	12 38 27.98	22 07 56.0	0.027	2000 Feb 14	Mosaic-N	Clouds
l2724bp696	272.4	69.6	12 10 05.92	9 13 01.4	0.019	1999 Apr 9	BTC	
l2751bp414	275.1	41.4	11 25 36.60	−16 47 13.5	0.041	1999 Apr 10	BTC	
l2752bm444......	275.2	−44.4	3 50 47.96	−61 52 06.6	0.026	1999 Oct 30	Mosiac-S	
l2778bp369	277.8	36.9	11 25 38.67	−21 44 58.7	0.038	2000 Apr 9	Mosaic-S	Clouds
l2790bp470	279.0	47.0	11 45 30.94	−12 47 07.9	0.034	1999 Apr 9	BTC	
l2797bp362	279.7	36.2	11 30 31.12	−22 59 40.6	0.044	1999 Apr 10	BTC	
l2808bp597	280.8	59.7	12 07 35.85	−1 16 28.6	0.021	1999 Apr 9	BTC	
l2815bp423	281.5	42.3	11 45 28.44	−17 48 36.2	0.033	2000 Apr 10	Mosaic-S	Clouds
l2822bp413	282.2	41.3	11 46 07.37	−18 55 38.8	0.041	1999 Apr 10	BTC	
l2843bp365	284.3	36.5	11 46 07.72	−23 59 51.3	0.064	2000 Apr 10	Mosaic-S	Clouds
l2881bp416	288.1	41.6	12 04 26.83	−19 54 52.0	0.051	1999 Apr 10	BTC	
l2897bp367	289.7	36.7	12 04 43.10	−24 58 06.3	0.084	2000 Apr 9	Mosaic-S	Clouds
l2900bp487	290.0	48.7	12 16 31.15	−13 17 34.7	0.051	1999 Apr 10	BTC	
l2914bp438	291.4	43.8	12 16 28.44	−18 17 14.8	0.071	2000 Apr 8	Mosaic-S	
l2924bp617	292.4	61.7	12 31 33.04	−0 45 51.8	0.027	1999 Apr 8	BTC	
l2927bp718	292.7	71.8	12 38 33.00	9 11 05.2	0.020	1999 Apr 8	BTC	
l2947bp669	294.7	66.9	12 38 31.25	4 14 05.8	0.032	2000 Apr 9	Mosaic-S	Clouds
l2977bp495	297.7	49.5	12 37 29.16	−13 13 47.8	0.049	1999 Apr 10	BTC	
l2979bp449	297.9	44.9	12 36 28.18	−17 49 31.6	0.037	1999 Apr 8	BTC	
l3016bp453	301.6	45.3	12 47 30.41	−17 33 41.6	0.042	1999 Apr 9	BTC	
l3018bp403	301.8	40.3	12 47 41.88	−22 33 48.6	0.079	2000 Apr 10	Mosaic-S	Clouds
l3023bp438	302.3	43.8	12 49 30.42	−19 04 09.7	0.066	2000 Apr 10	Mosaic-S	Clouds
l3023bp488	302.3	48.8	12 49 43.25	−14 04 10.6	0.054	1999 Apr 10	BTC	
l3036bp671	303.6	67.1	12 52 28.80	4 13 46.7	0.038	2000 Apr 9	Mosaic-S	
l3048bp561	304.8	56.1	12 55 38.01	−6 45 23.4	0.032	2000 Apr 8	Mosaic-S	
l3051bp608	305.1	60.8	12 55 40.21	−2 03 14.0	0.022	1999 Apr 10	BTC	
l3051bp611	305.1	61.1	12 55 37.78	−1 45 14.7	0.022	1999 Apr 8	BTC	
l3075bp809	307.5	80.9	12 54 28.42	18 03 18.8	0.028	2000 Feb 14	Mosaic-N	Clouds
l3114bp396	311.4	39.6	13 19 43.11	−22 48 22.5	0.116	2000 Apr 10	Mosaic-S	Clouds
l3164bp556	316.4	55.6	13 21 52.61	−6 28 25.4	0.042	2000 Apr 9	Mosaic-S	
l3177bp614	317.7	61.4	13 19 28.46	−0 39 54.8	0.026	1999 Apr 8	BTC	
l3201bp350	320.1	35.0	13 53 44.71	−25 47 09.3	0.069	2000 Apr 8	Mosaic-S	
l3220bp398	322.0	39.8	13 53 42.95	−20 45 16.5	0.076	1999 Apr 9	BTC	
l3236bp441	323.6	44.1	13 52 41.18	−16 17 59.6	0.101	2000 Apr 10	Mosaic-S	Clouds
l3251bm766......	325.1	−76.6	0 25 27.06	−39 23 19.1	0.016	1999 Oct 30	Mosiac-S	
l3258bp548	325.8	54.8	13 43 28.88	−5 44 39.8	0.026	2000 Apr 10	Mosaic-S	Clouds
l3261bp488	326.1	48.8	13 52 43.84	−11 17 41.9	0.057	1999 Apr 8	BTC	
l3263bp386	326.3	38.6	14 08 51.78	−20 43 58.7	0.079	1999 Apr 7	BTC	
l3291bm381......	329.1	−38.1	21 04 14.36	−65 29 48.0	0.029	1999 Apr 9	BTC	
l3301bp423	330.1	42.3	14 13 47.51	−16 11 09.1	0.080	2000 Apr 8	Mosaic-S	
l3311bm461......	331.1	−46.1	22 03 07.67	−60 45 40.4	0.038	1999 Apr 9	BTC	
l3331bp468	333.1	46.8	14 13 33.41	−11 12 18.4	0.064	1999 Apr 8	BTC	
l3335bp638	333.5	63.8	13 43 28.31	4 03 37.6	0.026	2000 Apr 9	Mosaic-S	
l3396bp682	339.6	68.2	13 43 21.33	9 06 22.9	0.026	1999 Apr 9	BTC	
l3401bp225	340.1	22.5	15 29 34.49	−28 43 56.6	0.440	2000 Apr 9	Mosaic-S	
l3430bm359......	343.0	−35.9	20 30 00.48	−54 59 36.9	0.048	1999 Apr 10	BTC	
l3431bp493	343.1	49.3	14 31 26.72	−5 36 42.5	0.052	2000 Apr 9	Mosaic-S	
l3432bp561	343.2	56.1	14 15 57.75	−0 00 58.7	0.040	2000 Apr 8	Mosaic-S	
l3440bm483......	344.0	−48.3	21 51 07.01	−51 53 20.5	0.022	1999 Oct 30	Mosiac-S	
l3443bm434......	344.3	−43.4	21 19 44.71	−52 59 45.5	0.023	1999 Apr 10	BTC	
l3469bm493......	346.9	−49.3	21 53 26.63	−49 45 52.8	0.028	1999 Apr 10	BTC	
l3479bp533	347.9	53.3	14 31 22.52	−0 36 48.7	0.046	1999 Apr 10	BTC	
l3501bp468	350.1	46.8	14 52 25.08	−4 41 29.8	0.090	2000 Apr 10	Mosaic-S	Clouds
l3518bp859	351.8	85.9	13 04 59.79	24 23 27.4	0.018	2000 Feb 14	Mosaic-N	Clouds
l3519bp550	351.9	55.0	14 34 04.08	2 12 03.2	0.038	2000 Apr 9	Mosaic-S	
l3538bm349......	353.8	−34.9	20 24 23.60	−46 10 57.7	0.032	1999 Oct 31	Mosiac-S	Clouds

TABLE 1—*Continued*

Name	l	b	R.A.[a]	Decl.[a]	$E(B-V)$	Date[b]	Instrument[c]	Conditions[d]
13549bp662......	354.9	66.2	14 07 05.51	11 17 57.5	0.024	1999 Apr 8	BTC	
13564bp511......	356.4	51.1	14 52 41.12	1 16 15.8	0.044	1999 Apr 9	BTC	

NOTES.—Units of right ascension are hours, minutes, and seconds, and units of declination are degrees, arcminutes, and arcseconds.
[a] J2000.0 coordinates.
[b] UT date. The data for each field observed with the Schmidt were obtained over several nights in 1998 October or November.
[c] BTC indicates the BTC camera mounted on the CTIO 4 m; Mosaic-N indicates the Northern Mosaic camera mounted on the KPNO 4 m; Mosaic-S indicates the Southern Mosaic camera mounted on the CTIO 4 m; B. Shmidt is the Burrell Schmidt at KPNO, owned and operated by Case Western Reserve University.
[d] Unless otherwise noted, conditions were photometric.

Thus, chip 1 for these observations actually corresponds to the traditional chip 2, while chip 2 is actually the traditional chip 1. For internal consistency we will refer to each chip by the number assigned during this observation run.

2.3. *Photometric Calibration*

It is essential that the data be photometrically calibrated. Candidate selection is based on specific color index criteria. Furthermore, distance estimates are based on the temperature index and magnitude. It is possible to select candidates based on relative positions in the color-color diagrams; however, such candidates will need to be calibrated to make them useful. Photometric standards for the Washington filter set (Geisler 1990, 1996) were observed on all photometric nights. The strategy was to place a standard field on every chip and in every filter at least once during each run to obtain zero-point offsets between the chips. In addition, standard fields were observed in all filters with a single chip throughout each night to obtain the color term and extinction coefficients.

Some of the fields were observed in nonphotometric conditions. Even if a photometric calibration solution is obtained for the instrument that took these data, the fields cannot be reliably calibrated without additional observations. We have plans to reobserve these fields with smaller telescopes, and we will publish these data when they are fully calibrated. We have spectroscopically confirmed giants in many of these fields, but, of course, do not know their distance.

The only run that was completely photometric was in 1999 April using the BTC camera. We discuss below the determination of this solution. We also have standard field observations for the Schmidt and Mosaic-S (Mosaic South on the CTIO 4 m; we will refer to the northern KPNO mosaic camera as Mosaic-N) taken under photometric conditions. However, we reserve discussion of these solutions until the full data set from these runs is published.

The photometric calibration solution for the BTC used three standard fields. Both SA 98 and SA 110 were observed with all four of the BTC chips, while NGC 3680 was observed only with chip 4. The photometric standard fields were observed over an air-mass range of 1.03 to 1.82, encompassing the air-mass range of the BTC target fields. A single calibration solution was used for all four nights. The data were examined for variations from night to night, but none were found to a precision of $\lesssim 0.005$ mag.

The photometric calibration solution took the form

$$M = m + Z_m - 0.1424 \times X + 0.1538 \times (m - t_2) \pm 0.020 \text{ (62 stars)} , \quad (1a)$$

$$C - M = Z_{cm} - 0.2052 \times X + 1.043 \times (c - m) \pm 0.023 \text{ (63 stars)} , \quad (1b)$$

$$M - T_2 = Z_{mt_2} - 0.09551 \times X + 1.158 \times (m - t_2) \pm 0.017 \text{ (61 stars)} , \quad (1c)$$

$$M - 51 = m - 51' + Z_{m51} + 0.0107 \times X + 0.1655 \times (m - t_2) \pm 0.018 \text{ (65 stars)} , \quad (1d)$$

where M, C, T_2 and 51 correspond to calibrated magnitudes; m, c, t_2 and $51'$ correspond to instrumental magnitudes; X is the air mass; and Z is the zero point. The color terms and the extinction terms were determined using the observations of chip 4; no significant differences were found among the color terms of the other chips. The rms residuals and the number of stars used in the fit are listed to the right of the equations above. A zero-point offset was then determined for each of the other chips. The zero points are listed in Table 3. There were five to 10 stars available for the fit of each chip offset. The rms residual ranged from 0.015 to 0.025.

The final step in our photometric calibration process is to remove interstellar reddening. For this purpose we have used the reddening maps of Schlegel et al. (1998) to estimate the reddening toward each star. The extinction values for each filter were derived from the relations given in Harris & Canterna (1979) and Geisler (1984). These relations are

$$\frac{A_C}{E(B-V)} = 4.71 , \quad (2a)$$

$$\frac{A_M}{E(B-V)} = 3.64 , \quad (2b)$$

$$\frac{A_{51}}{E(B-V)} = 3.61 , \quad (2c)$$

$$\frac{A_{T2}}{E(B-V)} = 2.05 , \quad (2d)$$

assuming $R_V = 3.3$. These are high-latitude fields, and the reddening is quite low by design (see § 2.1) so errors due to differential reddening are not significant. In addition, the $M-51$ index is almost reddening-free.

3. PHOTOMETRIC PIPELINE

The processing pipeline for this survey has four main tasks: (1) to organize the images and associated data files, (2) to apply instrumental calibration to the images, (3) to measure stellar photometry from the images, and (4) to record relevant information about each of these steps.

TABLE 2

OBSERVATION SUMMARY

	M			C			DDO51			T_2		
NAME	Time[a]	Air Mass	FWHM[b]	Time[a]	Air Mass	FWHM[b]	Time[a]	Air Mass	FWHM[b]	Time[a]	Air Mass	FWHM[b]
l0034bp541	100	1.249	1.4	500	1.257	1.4	600	1.269	1.5	120	1.251	1.2
l0037bp613	140	1.561	1.3	700	1.504	1.3	350	1.582	1.2	170	1.623	0.9
l0055bp488	100	1.447	1.0	500	1.395	1.2	600	1.354	1.0	120	1.427	1.0
l0064bm190......	50	1.028	1.2	250	1.019	1.3	300	1.014	1.3	60	1.024	1.1
l0111bp440	100	1.233	1.4	500	1.223	1.6	600	1.217	1.5	120	1.228	1.1
l0118bp517	100	1.372	1.0	500	1.350	1.2	250	1.395	1.0	120	1.385	0.9
l0171bp467	100	1.482	1.2	500	1.445	1.3	250	1.496	1.1	120	1.522	1.0
l0182bp470	100	1.776	1.4	500	1.684	1.7	600	1.612	1.5	120	1.739	1.3
l0420bm414......	120	1.124	1.5	560	1.176	1.8	500	1.139	1.8	140	1.142	1.8
l0481bp813	100	1.005	0.9	500	1.003	1.2	450	1.001	1.1	120	1.001	1.1
l0592bp857	100	1.001	1.0	500	1.003	1.1	450	1.006	1.2	120	1.009	1.0
l0645bp855	100	1.036	0.8	500	1.044	0.9	450	1.059	0.9	120	1.070	0.8
l0658bp855	100	1.031	0.9	500	1.024	1.0	450	1.016	1.0	120	1.011	0.8
l0820bm610......	120	1.116	1.9	560	1.132	2.2	500	1.122	2.5	140	1.142	2.5
l0900bm450......	32 ×			14 ×			11 ×			7 ×		
l0915bm698......	180	1.210	1.6	840	1.298	2.1	750	1.242	1.9	210	1.345	2.8
l1000bm500......	7 ×			7 ×			6 ×			7 ×		
l1124bm666......	120	1.111	1.8	560	1.118	1.7	500	1.113	2.2	140	1.123	2.3
l1200bm400......	7 ×			8 ×			9 ×			4 ×		
l1300bm500......	14 ×			8 ×			7 ×			7 ×		
l1350bm400......	11 ×			13 ×			9 ×			9 ×		
l1379bm417......	100	1.561	1.1	500	1.581	1.2	450	1.567	1.3	120	1.594	1.5
l1390bm570......	120	1.217	1.5	560	1.218	1.7	500	1.216	1.7	240	1.227	2.1
l1450bp300	13 ×			6 ×			9 ×			5 ×		
l1550bm470......	6 ×			6 ×			8 ×			6 ×		
l1828bp240	150	1.017	3.0	750	1.012	3.0	575	1.006	2.2	180	1.004	1.7
l1850bm450......	13 ×			15 ×			9 ×			12 ×		
l1861bm475......	100	1.142	1.1	500	1.126	1.2	450	1.135	1.2	120	1.122	1.3
l1862bm470......	180	1.124	2.6	840	1.118	2.0	750	1.120	2.8	210	1.128	3.3
l1886bp302	150	1.000	1.5	750	1.002	2.1	575	1.006	2.0	180	1.010	1.7
l1994bm354......	180	1.104	2.8	840	1.101	3.3	750	1.101	3.3	210	1.106	3.2
l2035bp460	100	1.008	0.8	625	1.006	0.8	580	1.007	0.8	150	1.008	0.9
l2045bp424	150	1.045	1.4	750	1.035	2.0	575	1.024	2.4	180	1.018	2.2
l2090bp517	100	1.011	0.8	500	1.011	0.8	450	1.012	0.7	120	1.014	0.7
l2092bm457......	100	1.036	1.1	500	1.049	1.1	450	1.041	1.2	120	1.057	1.5
l2102bp592	100	1.011	0.8	500	1.009	0.9	450	1.008	0.8	120	1.009	0.8
l2144bp643	100	1.010	0.8	500	1.011	0.8	450	1.013	0.8	120	1.016	0.7
l2179bp376	100	1.361	1.0	500	1.360	1.0	300	1.362	1.0	120	1.366	0.9
l2203bm428......	120	1.052	1.5	600	1.030	1.4	540	1.042	1.3	160	1.022	1.3
l2211bm357......	110	1.047	1.3	550	1.028	1.4	500	1.038	1.5	140	1.022	1.4
l2223bm477......	120	1.294	1.7	600	1.102	1.6	540	1.129	1.6	160	1.085	1.8
l2233bp433	100	1.350	1.0	500	1.342	1.0	300	1.354	0.9	120	1.363	0.8
l2235bp354	100	1.293	2.0	500	1.278	2.2	600	1.269	2.0	120	1.287	1.5
l2291bm501......	100	1.000	1.1	500	1.003	1.1	450	1.001	1.1	120	1.006	1.3
l2297bp469	100	1.291	1.1	500	1.291	1.1	250	1.291	1.0	120	1.292	0.9
l2321bp249	100	1.451	1.3	500	1.364	1.4	450	1.413	1.5	120	1.331	1.8
l2326bp246	100	1.109	0.8	500	1.110	0.8	300	1.108	0.8	120	1.107	0.8
l2328bm252......	120	1.380	1.5	600	1.286	1.6	540	1.339	1.6	160	1.251	1.7
l2336bm321......	100	1.002	1.1	500	1.000	1.4	450	1.001	1.2	120	1.001	1.3
l2341bp321	100	1.143	1.3	500	1.141	1.0	300	1.147	1.0	120	1.150	0.8
l2342bp539	100	1.313	0.9	500	1.316	1.0	300	1.312	0.9	120	1.313	0.8
l2371bp218	100	1.069	1.5	500	1.090	1.7	600	1.105	1.6	120	1.071	1.2
l2373bp416	100	1.176	0.8	500	1.176	0.9	300	1.176	0.8	120	1.177	0.8
l2376bp354	100	1.133	0.9	500	1.134	1.0	300	1.132	0.9	120	1.132	0.8
l2376bp585	100	1.334	1.3	500	1.336	1.2	250	1.333	1.0	120	1.332	0.8
l2410bp534	100	1.249	1.3	500	1.251	1.6	600	1.257	1.5	120	1.249	1.4
l2432bp438	100	1.152	0.9	500	1.152	1.0	300	1.153	0.9	120	1.155	0.8
l2441bp375	100	1.118	1.2	500	1.110	1.2	600	1.106	1.1	120	1.115	1.1
l2449bp632	100	1.346	0.9	500	1.338	1.0	300	1.349	0.9	120	1.357	0.8
l2468bm314......	100	1.020	1.1	500	1.022	1.2	450	1.020	1.2	120	1.024	1.2
l2481bp300	100	1.051	0.8	500	1.054	0.8	300	1.050	0.8	120	1.050	0.7
l2522bp266	120	1.025	1.1	750	1.028	1.8	720	1.036	1.6	145	1.026	1.1
l2524bp528	100	1.174	0.9	500	1.171	1.0	300	1.175	0.9	120	1.179	0.9
l2525bp597	100	1.251	1.3	500	1.244	1.4	600	1.241	1.2	120	1.248	1.1

TABLE 2—*Continued*

Name	M Time[a]	M Air Mass	M FWHM[b]	C Time[a]	C Air Mass	C FWHM[b]	DDO51 Time[a]	DDO51 Air Mass	DDO51 FWHM[b]	T_2 Time[a]	T_2 Air Mass	T_2 FWHM[b]
12574bp405	100	1.075	0.8	500	1.069	0.9	300	1.078	0.8	120	1.083	0.8
12586bp483	100	1.110	1.4	500	1.116	1.7	600	1.126	1.5	120	1.112	1.3
12611bp668	100	1.387	0.9	500	1.397	1.0	300	1.371	1.0	120	1.361	0.9
12634bp567	100	1.184	0.8	500	1.189	0.9	300	1.177	0.8	120	1.174	0.8
12637bp330	100	1.019	0.9	500	1.019	0.9	250	1.019	0.8	120	1.020	0.7
12638bp423	125	1.067	1.1	620	1.060	1.1	310	1.071	0.9	150	1.150	0.9
12676bp626	100	1.209	1.1	500	1.213	1.2	600	1.220	1.1	120	1.210	1.0
12682bp361	100	1.020	0.9	500	1.020	1.0	300	1.021	0.9	120	1.022	0.9
12690bp580	100	1.209	0.9	500	1.216	0.9	300	1.198	0.9	120	1.192	0.9
12713bp319	100	1.008	1.5	500	1.006	1.6	600	1.007	1.5	120	1.007	1.7
12715bp289	120	1.030	1.0	600	1.018	1.1	720	1.010	1.2	145	1.025	8.3
12717bp842	100	1.087	0.9	500	1.075	1.0	450	1.060	0.8	120	1.044	0.9
12724bp696	100	1.402	0.9	500	1.376	1.0	300	1.412	1.0	120	1.434	0.8
12751bp414	100	1.034	0.9	500	1.030	1.0	300	1.035	0.9	120	1.039	0.9
12752bm444......	100	1.187	1.2	500	1.179	1.2	450	1.183	1.3	120	1.177	1.4
12778bp369	110	1.016	1.3	550	1.023	1.5	660	1.033	1.4	132	1.018	1.1
12790bp470	100	1.328	1.1	500	1.286	1.2	300	1.344	1.1	120	1.377	0.9
12797bp362	100	1.025	0.9	500	1.028	0.9	300	1.020	0.8	120	1.018	0.8
12808bp597	100	1.300	1.0	500	1.312	1.0	300	1.279	1.0	120	1.268	0.9
12815bp423	100	1.038	1.2	500	1.049	1.2	600	1.062	1.2	120	1.042	1.1
12822bp413	100	1.092	0.8	500	1.076	0.9	300	1.099	0.8	120	1.112	0.8
12843bp365	100	1.016	1.3	500	1.010	1.7	600	1.007	1.5	120	1.013	1.2
12881bp416	100	1.102	0.9	500	1.109	1.0	300	1.089	0.9	120	1.083	0.8
12897bp367	110	1.031	1.4	550	1.020	1.7	660	1.012	1.4	132	1.027	1.3
12900bp487	100	1.167	0.9	500	1.144	0.9	300	1.176	0.9	120	1.195	0.8
12914bp438	100	1.037	1.0	500	1.029	1.0	600	1.024	1.0	120	1.034	0.9
12924bp617	100	1.147	1.0	500	1.147	1.1	250	1.148	1.0	120	1.149	0.9
12927bp718	100	1.321	1.3	500	1.327	1.3	250	1.314	1.0	120	1.309	0.9
12947bp669	110	1.218	2.2	550	1.228	2.0	660	1.243	1.9	132	1.221	1.8
12977bp495	100	1.468	1.0	500	1.410	1.0	300	1.491	0.9	120	1.537	0.9
12979bp449	100	1.027	1.0	500	1.024	1.1	250	1.029	1.0	120	1.032	1.0
13016bp453	100	1.194	1.0	500	1.166	1.0	300	1.205	0.9	120	1.227	0.8
13018bp403	100	1.025	1.2	500	1.017	1.4	600	1.012	1.4	120	1.022	1.5
13023bp438	100	1.039	1.2	500	1.052	1.5	600	1.072	1.2	120	1.044	1.1
13023bp488	100	1.285	0.9	500	1.299	1.0	300	1.259	0.9	120	1.245	0.8
13036bp671	100	1.213	1.5	500	1.219	1.6	600	1.229	2.2	120	1.215	1.3
13048bp561	100	1.121	0.9	500	1.105	1.1	500	1.097	1.1	120	1.116	0.8
13051bp608	100	1.738	1.1	500	1.773	1.2	300	1.680	1.0	120	1.645	0.9
13051bp611	140	1.176	1.0	700	1.160	1.1	350	1.183	1.1	170	1.196	1.1
13075bp809	100	1.226	1.0	500	1.202	1.0	450	1.173	0.9	120	1.154	0.9
13114bp396	200	1.082	1.2	500	1.054	1.3	600	1.040	1.2	120	1.072	1.5
13164bp556	100	1.131	1.3	500	1.183	1.0	600	1.211	1.0	120	1.159	0.9
13177bp614	110	1.199	1.1	540	1.205	1.2	270	1.189	1.1	130	1.183	1.0
13201bp350	100	1.003	1.0	500	1.005	1.0	600	1.010	1.0	120	1.004	0.9
13220bp398	100	1.224	0.9	500	1.237	1.0	300	1.202	1.0	120	1.190	0.8
13236bp441	120	1.071	1.3	500	1.089	1.2	600	1.109	1.2	120	1.077	1.2
13251bm766......	100	1.016	1.1	500	1.021	1.2	450	1.027	1.2	120	1.018	1.4
13258bp548	150	1.484	1.4	750	1.397	1.4	900	1.330	1.3	180	1.451	1.5
13261bp488	110	1.092	1.0	540	1.080	1.1	270	1.097	1.0	130	1.106	0.9
13263bp386	100	1.499	1.5	500	1.384	1.5	250	1.442	1.3	120	1.569	1.1
13291bm381......	100	1.521	1.2	500	1.510	1.1	300	1.543	1.1	120	1.556	1.1
13301bp423	100	1.051	1.1	500	1.041	1.3	600	1.035	1.0	120	1.047	1.0
13311bm461......	100	1.617	1.0	500	1.664	1.2	300	1.601	0.9	120	1.571	0.9
13331bp468	120	1.374	1.0	580	1.394	1.1	290	1.339	1.0	140	1.320	0.8
13335bp638	100	1.217	1.7	500	1.211	1.7	600	1.209	1.9	120	1.215	1.2
13396bp682	100	1.458	1.2	500	1.483	1.1	300	1.434	1.1	120	1.421	0.8
13401bp225	100	1.116	1.0	500	1.146	1.1	600	1.178	1.1	120	1.126	0.9
13430bm359......	100	1.372	1.0	500	1.360	1.1	300	1.395	1.0	120	1.409	0.9
13431bp493	100	1.227	0.9	500	1.265	1.1	600	1.304	1.0	120	1.240	0.7
13432bp561	100	1.608	1.4	500	1.459	1.4	600	1.525	1.3	120	1.705	1.3
13440bm483......	100	1.389	1.2	500	1.462	1.2	450	1.418	1.4	120	1.299	1.6
13443bm434......	100	1.443	1.1	500	1.486	1.1	300	1.429	1.1	120	1.402	1.0
13469bm493......	100	1.459	1.1	500	1.443	1.2	300	1.491	1.0	120	1.511	1.0
13479bp533	100	1.356	0.9	500	1.320	1.0	300	1.370	0.9	120	1.399	0.8
13501bp468	150	1.244	1.5	750	1.295	1.5	900	1.358	1.4	180	1.261	1.3

TABLE 2—*Continued*

Name	M Time[a]	M Air Mass	M FWHM[b]	C Time[a]	C Air Mass	C FWHM[b]	DDO51 Time[a]	DDO51 Air Mass	DDO51 FWHM[b]	T_2 Time[a]	T_2 Air Mass	T_2 FWHM[b]
l3518bp859	100	1.049	0.9	500	1.060	1.0	450	1.075	0.9	120	1.090	1.0
l3519bp550	100	1.310	1.0	500	1.227	1.0	600	1.211	0.9	120	1.258	0.9
l3538bm349	120	1.136	1.4	560	1.174	1.9	500	1.150	1.6	140	1.193	1.7
l3549bp662	100	1.421	1.0	500	1.431	1.2	250	1.406	1.1	120	1.397	1.0
l3564bp511	100	1.348	1.0	500	1.315	1.1	300	1.361	1.0	120	1.388	1.1

[a] Time given in seconds. Fields observed with the B. Schmidt telescope have multiple exposures, each of length 1200 s. Listed in the table are the number of exposures, followed by a times cross.

[b] The average FWHM, in arcseconds, over all chips.

Because of the large amount of data, it is also crucial that this process is flexible enough to be stopped and started at any point. This allows us, for example, to perform some of the processing during the observing run and finish the processing at our home institutions. Finally, we require the process to be robust against computer crashes, missing header information, and other inevitable mishaps that arise during an observing run. Elements of our approach follow the OGLE pipelines.

The essence of our pipeline is to maintain a flag file for each image. We chose to keep a separate flag for each chip in the mosaic field, although it is possible to maintain a single flag for all the chips of a given exposure. This flag file stores information needed by each step in the pipeline, namely, the location of the image in the computer system and the current reduction state of the image. The former is simply data stored in the file itself, while the latter is indicated in the flag file name. For instance, suppose image SPAG001.FITS has been flat-fielded and photometered, while SPAG002.FITS has only been flat-fielded. The corresponding flag files might be SPAG001.PHOT and SPAG002.FLAT. This system allows one to glance at a directory of files and know immediately the progress of the pipeline.

We have split each step of the process into a separate program or script. These are designed to run continuously as daemon processes. Each daemon scans the directory of flag files for images that are ready for its step in the process. When such an image is found, it is processed, the flag file is updated, and a log file is appended with information about the image relevant to that step. A separate log is maintained by each of the daemons. Because the pipeline is so modular, it is easy to modify or even skip steps without affecting other steps in the process.

Figure 3 is a flowchart representation of the reduction process. The shaded region is the instrumental calibration branch. These processes are not automated and must be completed before the third daemon can run. A full description of the instrumental calibration steps is discussed in § 3.3. In addition, photometric calibration and astrometry determinations are not currently automated. We are working on automating the astrometry process.

TABLE 3

Zero Points for Calibration Solution

Chip	Z_m	Z_{cm}	Z_{mt_2}	Z_{m51}
1......	25.0311	−1.2813	1.0855	2.4780
2......	25.3346	−1.0666	1.2429	2.4498
3......	25.2730	−1.0567	1.2126	2.4592
4......	25.3753	−1.1050	1.3238	2.4716

3.1. *Daemon 1: Pipeline Initiation*

The first daemon initiates an image into the pipeline by creating a flag file and copying the image to the working area. Since the flag files do not yet exist, this daemon must rely on other clues to determine when an image is ready to be processed. For instance, if the images are being processed during the observing run, this daemon can scan the acquisition directory and process any new images that appear. The indications that an image is ready are instrument dependent. One can use the size of the image file, but only if the instrument does not preallocate the memory for this file at the beginning of readout. To overcome this, once an image file appears the daemon can wait for a delay time that is at least as long as the readout time.

3.2. *Daemon 2: Organization*

Most often the names generated by the instrument have a prefix and a running number, such as SPAG005. The second daemon organizes the images with convenient names and directories so that images from the same field are grouped together. This daemon renames the file and copies it to the appropriate directory for the field, creating the directory if necessary. A log is created for translating between the original name and the new name. Finally, the new name is placed in the flag file so that subsequent daemons know the location of the file.

For our survey, the adopted naming convention is: *l*[*longitude*]*b*[*p/m*][*latitude*]_[*chip*]_[*filter*]_[*number*]. Bracketed information is variable and image specific. We found that the nearest degree for longitude and latitude was not quite accurate enough to uniquely distinguish different fields. Hence, the nearest tenth of a degree is placed in the name, with no decimal point. The sign of the latitude is indicated by "p" for the northern Galactic hemisphere and "m" for the southern Galactic hemisphere. The filter is given a letter code ("M" for M, "G" for DDO51, "I" for T_2, and "C" for C), and a reference number. The reference number is necessary because our survey uses several different telescopes, which can have different filter sets, and, thus, substantially different color terms from run to run. Thus it is necessary to distinguish the T_2 filter of one instrument from the T_2 filter of another. Finally, there may be more than one image with the same filter in a given field. A running number is appended to the end to distinguish these images. As an example, consider the second exposure of

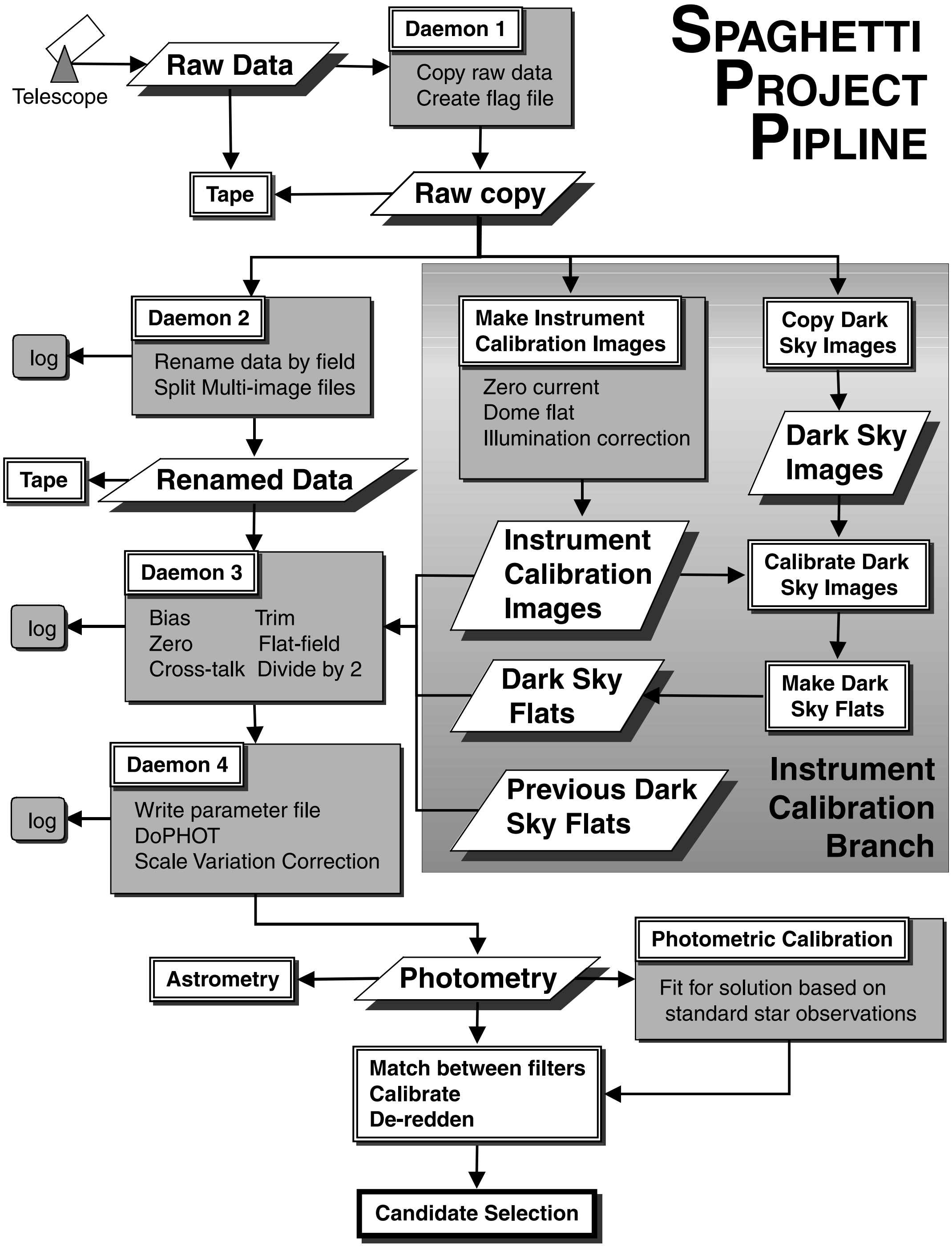

FIG. 3.—Flow chart representation of our reduction process. The instrumental calibration branch is not automated and must be completed before daemon 3 can run.

chip 4 from a field at $l = 100.1$ and $b = -45.5$, with an M filter from the filter set with reference code 1. This would have the name l1001bm455_4_M1_2.fits.

Position, filter, and chip information are read from the header. In those cases where the header information is missing, the daemon stops and queries the user to enter the information by hand. There are also cases where images from the same field can be given slightly different names. If the coordinates of different exposures are different by just enough to change the nearest tenth of a degree in either Galactic latitude or longitude, the names will be different. An additional program was necessary to correct the names of such images. This program changes the name, updates the logs to reflect the change, and copies the image and associated data files to the correct field directory.

The images from each chip of the Mosaic cameras are grouped together in a single FITS file when read from the instrument. Subsequent steps in our pipeline work with single image files. This daemon was modified to split the group file into a separate file for each chip.

3.3. *Daemon 3: Instrumental Calibration*

The third daemon applies the instrumental calibration to the images. This includes trimming the images, subtracting the bias, subtracting the zero-current, applying a flat-field correction, applying an illumination correction, and applying a dark sky flat correction. Creation of these instrumental calibration images, as described below, is not automated (see Fig. 3).

In addition, the instrumental calibration images must be completed before this daemon can run. This presents some limitations in our ability to achieve true real-time reduction at the telescope. The most problematic are the dark sky flats, because these come from the target images themselves. We have found that dark sky flats are essential for the Mosaic cameras to obtain the best photometry. We are currently testing the reliability of reusing certain calibration images, especially the dark sky flats, from previous runs with the same instrument.

This daemon was originally written as an IRAF[3] script to take advantage of the many routines that exist to process images. We have subsequently written a stand-alone program to perform these processes. We achieve an 8-fold speed increase over the IRAF script due to optimizing disk access. This speed increase is imperative to achieve real-time reduction.

The BTC data were processed with the IRAF script. In this case the overscan region of each line was averaged along the readout direction. A first order Legendre polynomial was then fitted to these average values. Points which deviated by more than 3 standard deviations were eliminated from the fit. The evaluation of this smooth fit determined the bias level subtracted from each line of the image. The algorithm used in all other data sets does not use a smooth fit for the bias subtraction. Instead, the bias for each row was determined separately from the average of the overscan region for that row. This later algorithm is also the one used in our stand-alone program. We found this to work better for the Schmidt and Mosaic cameras. There was no significant difference between the two algorithms for BTC images.

Zero-current images are averaged together after being trimmed and bias subtracted. Flat-field images are created from dome flats. They are trimmed, bias subtracted, zero subtracted, and median combined to form a single image for each chip and each filter.

Illumination corrections are made from twilight sky flat images. The twilight images are trimmed, bias subtracted, zero subtracted, flat-field corrected, and median combined. A polynomial with order between 3 and 5 is then used to fit the large-scale structure, producing an illumination correction. The exact order of the fit varies depending on instrument and is chosen as low as possible while still reasonably matching the large-scale structure.

When combining these instrumental calibration images, they must first be scaled. A significant number of extreme value pixels, from cosmic rays or bad pixels, can alter the statistics of the image. These same extreme values also affect the illumination correction fits adversely. Therefore, if necessary, we replace these extreme values with more appropriate values, such as zero, or the saturation level.

Finally dark sky flats are made from target data. In the case of the 1999 April BTC data, the target images taken on the first two nights (April 6 and 7) were used. The target data are first processed normally, including being trimmed, bias subtracted, zero subtracted, flat-field corrected, and illumination corrected. The images are then median combined. The median images are examined to be sure all objects are adequately removed. If the objects are not removed, clipping is applied during the median combination.

This dark sky flat also serves to remove the fringe pattern in the T_2 images. The fringing level is a small fraction of the sky, which allows one to represent the fringe as fringe $= \epsilon \times$ sky, where $\epsilon \ll 1$ and is approximately constant. Thus, the net count in the image is sky + fringe = sky$(1 + \epsilon)$. The fringe pattern has been stable within a given observing run for the instruments we have used. Thus, the normalized dark sky flat contains $(1 + \epsilon)$. Division of target images by the dark sky flat leaves just *sky*.

The assumption that ϵ is constant is only approximately true. However, because $\epsilon \ll 1$, small changes in ϵ lead to even smaller errors in the fringe removal. For example, if ϵ is the dark sky value, while ϵ' is the target image value, the ratio $(1 + \epsilon')/(1 + \epsilon) = 1 + (\epsilon' - \epsilon)/\ (1 + \epsilon)$. Thus, if ϵ' is 10% different from ϵ, the fringe correction error is approximately 0.1ϵ, which is very small since $\epsilon \ll 1$.

It was found that the BTC data did not require a dark sky correction, with the exception of fringe removal. The magnitude of the dark sky correction indicates how well the dome and twilight images flat-field the data, as well as provides an indication of flat-field variability. The standard deviation of this correction in the central quarter of each of the BTC chips was 0.7%, 0.6%, 1.4%, and 0.5% in C, M, DDO51, and T_2, respectively. These small corrections indicate the chips are remarkably stable, leading to high-quality photometry.

Stellar photometry is performed with the DoPHOT (Schechter, Mateo, & Saha 1993) program (see § 3.4). The version of DoPHOT used so far in this survey requires the image data to be 2 byte integers. This restricts the count values to $\lesssim$32,000. The saturation level is typically larger than this by a factor of 2. To maintain this dynamic range, the image values are reduced by a factor of 2 before they are converted to 2 byte integers. The gain is then effectively twice the previous value. After division by two the noise in the images was still well sampled.

3.3.1. *Mosaic Cameras*

Both Mosaic instruments received significant benefit from the dark sky flat, in addition to fringe removal. This necessity makes it difficult to achieve true real-time processing because many target images are needed before a dark sky flat can be constructed. For future runs we will be testing the possibility of using dark sky flats made from images taken in previous runs. The success of this will depend on the long-term stability of the instruments, including the fringe pattern.

In addition to the basic reduction steps described above, the Mosaic cameras require the removal of cross-talk between amplifiers of adjoining pairs of chips. Properly removing this effect requires calibrating two chips simulta-

[3] IRAF is distributed by the National Optical Astronomy Observatories, operated by the Association of Universities for Research in Astronomy, Inc., under cooperative agreement with the National Science Foundation.

neously. This can be done with IRAF and has been implemented in our stand-alone processing code.

3.3.2. *Schmidt Camera*

Prior to being instrumentally calibrated, the Schmidt images require some preprocessing. First, the data values are saved by the instrument as type short, but actually have the full range of unsigned short by using negative values. Thus, the data have to be converted to unsigned short and then floating point to be processed properly.

Second, while the saturation level is constant across the chip, the illumination is not. There is a large flat-field correction at the edges compared with the center because of vignetting. Thus, after flat-fielding the images, there is a large variation in the effective saturation level. Current versions of DoPHOT only allow a single saturation level for each chip. Unsaturated, but bright, stars away from the center of the chip are pushed above the saturation level by the flat-field correction.

If the saturation level is chosen appropriately for the center of the chip, these bright stars are flagged as saturated and ignored by DoPHOT. These bright stars are needed to define the PSF shape and aperture corrections in the outer regions of the chip. This is critical because the PSF is variable. On the other hand, if the saturation is chosen appropriately for the outer regions of the chip, saturated stars in the center are accepted as unsaturated resulting in inaccurate photometry and misguided PSF fits.

To overcome this problem, we adjust the saturation level prior to flat-fielding the images, but after converting to type float. All values greater than the saturation level are set to an extremely high value. This value must be larger than the saturation level near the edges after the flat-field correction is applied. When the data are converted to 2 byte integers for DoPHOT, these extremely high values are set to the maximum allowed value to ensure they will be flagged by DoPHOT as saturated.

In principle, we could apply this same technique to data from the BTC and Mosaic cameras as well. However, the vignetting for these instruments is less severe than the Schmidt's, and the flat-field correction varies less across a single chip ($\sim 10\%$). Thus, by setting the saturation level to the lowest effective value, we miss only a few of the brightest unsaturated stars.

Finally, because of the large field of view of the Schmidt camera, it is difficult to obtain good dome flat images. Instead, we relied on twilight sky images for the flat-field correction. These are processed identically to other twilight sky flats as described above, except we do not fit a smooth function to the combined image.

3.4. *Photometry Measurement*

The final daemon measures stellar photometry from the instrumentally calibrated images. We use the program DoPHOT (Schechter et al. 1993) for this measurement. The first step is to create a parameter file for the image. The parameters must include an estimate for the FWHM and the sky level. We wrote a program to estimate these values and output a parameter list appropriate for DoPHOT. The sky is estimated as the median pixel value.

The FWHM is estimated by finding local maxima in the image and measuring the width at half the peak value. This is done only in one dimension to save computational time. The median value of these widths is used as the estimate. Because this estimate works in only one dimension, some care is needed in restricting the allowed range of widths. Permitting narrow widths, as from cosmic rays or bad pixels, produces a FWHM estimate that is too small. Permitting wide widths from a large number of background galaxies or saturated stars produces a FWHM estimate that is too large. These limits have to be adjusted as the seeing varies. Thus, the PSF determined by DoPHOT is monitored carefully to ensure that the FWHM estimate does not lead the program astray.

We set the object detection threshold to 2.5 times the noise standard deviation above the background. The PSF parameters are allowed to vary with the third power of position. The variations are small for the BTC, less than 10% from center to corner within a single chip.

We use an aperture radius of 12 pixels ($5\farcs2$) for determining aperture corrections. This radius was constrained by two factors. First, the aperture must be sufficiently large to contain all the flux from the star. This can be determined by plotting the aperture photometry as a function of radius. The aperture photometry will converge to a constant value, within the background noise, as the radius increases. Second, the aperture should be as small as possible to minimize the noise contribution from the background and neighboring stars.

We have added a routine to DoPHOT for automatically determining and applying aperture corrections. We found that the functional form of the aperture correction position variation was the same for the full aperture as it was for smaller apertures, provided the smaller aperture enclosed the stellar core. The only difference between the smaller aperture function and the full aperture function was a constant additive offset. In effect, the aperture correction did vary across a chip, and the shape of this variation could be determined from any aperture (within bounds). Therefore, the functional form of the position variation was determined by using a smaller, and hence less noisy, aperture. The aperture correction function determined from this smaller aperture was then corrected to a larger aperture with a constant offset.

The aperture corrections are determined with a third-power positional fit. Only stars with internal errors better than 0.04 mag are used in this fit. To reduce the noise in the fit, the least squares determination was made with an aperture radius of $3\farcs6$. A constant offset was applied to obtain the $5\farcs2$ radius correction. The same procedure is applied to other data sets with similar aperture sizes.

The photometry must also be corrected for variable pixel scale. DoPHOT works best when the background is truly flat. Therefore, we allow the flat-field process to make the background flat before doing photometry. However, because the pixel scale varies across the field, photometric calibration of point sources will be in error systematically between the center and edge of the field. The correction varies smoothly and slowly compared with the PSF size. Therefore, we can apply this correction directly to the photometry. Care must also be taken to apply the same correction to standard star observations.

Scale variation solutions for both Mosaic instruments are available with the MSCRED IRAF reduction package. We also have a scale variation solution for the BTC derived from observations of UNSO standard fields (P. Fischer 2000, private communication). The camera on the Burrell Schmidt does not have significant pixel area variation.

Once the final photometry is obtained for all four filters, the stars are matched and calibrated. The star lists of each filter are matched to within a 0.5 pixel radius. All stars with multiple matches within this radius are rejected. The photometric calibration solution is then applied. In order for the color term to be applied, the star must be detected in both the M and T_2 filter. The stars do not have to be detected in C or DDO51. Such stars will not be selected as halo giant candidates, although they could be selected among the blue halo candidates.

3.4.1. *Schmidt Photometry*

The eight fields obtained with the Schmidt require a more complicated scheme. Prior to matching between filters, the stellar photometry from all of the images in a single filter are matched and averaged. The images are often taken on different nights, so the pointing can vary from image to image. Thus, a master image is chosen, and all star list coordinates are transformed to this system.

The master also serves as a photometric master. When averaging photometry they must be on the same calibration system. The zero point can vary from image to image because of clouds or differences in air mass. A photometric zero-point difference is measured and applied to each frame to put them on the same photometric system as the master image. Finally, only stars that were found on $\sim$80% of the images are retained.

In addition to averaging the photometry, the coordinates are also averaged. The coordinates from each star list are transformed to the coordinate system of the master image. The transformation is fit with equations of the form

$$x' = \delta x + a_x x + b_x y \, , \tag{4a}$$

$$y' = \delta y + a_y x + b_y y \, , \tag{4b}$$

where x' and y' are coordinates in the master system, and δx and δy are constants. With all the coordinates in the same system, the coordinates of each star are averaged together. This is necessary to improve positional accuracy because of the large pixels of this camera.

3.5. *Astrometry*

We determined astrometry solutions using the IRAF package FINDER. The USNO-A2 catalog[4] was used as a reference for the solution. Unfortunately, the position information written to the image headers of the BTC files was not consistent. It varied randomly from the true pointing by several arcminutes. Thus, we were forced to find a solution for each chip of each field separately.

The number of reference stars on each chip varied greatly with field position, ranging from <200 to >1000. Because of this, the accuracy of the solution varied greatly. In the low-density regions the residual rms from the fit was $\sim 0\farcs5$, but it was as good as $\sim 0\farcs2$ in the high-density regions. The position information presented in § 4 should not be considered accurate enough for fiber spectroscopy. However, it is good enough to uniquely identify each star. We are working on an automated process for determining the astrometric solutions.

The images taken with the Schmidt camera are often deep enough that many astrometric standard stars are saturated. Thus, to achieve an accurate astrometric solution we take several short exposures in M of each field. We average the coordinates of stars detected on these short exposures, as we did for the deeper images described in § 3.4.1. This allows us to find an astrometric solution which can be tied to the master frame of the deeper images. This hybrid procedure has produced superb results which have been successfully used with fiber spectroscopes. Further details of these astrometry calculations will be described in a later paper that discusses our fiber spectroscopy. However, it is worth noting that, ultimately, the solution accuracy is limited by the unknown proper motions of stars in the USNO-A2 catalog.

4. PHOTOMETRY RESULTS

Table 4 lists stars from the 53 BTC fields. The complete list of stars with errors <0.04 can be accessed in the electronic version of this paper, as well as through ADC.[5] Data sets from other observing runs have not yet been fully photometrically calibrated because of problematic weather. As these data sets are calibrated, we will add them to the ADC database and describe them in subsequent papers in this series.

We found that the photometry from the BTC chip 1 (our notation; traditional chip 2) is not as reliable as that from the other three chips. This chip contained a residual flat-field pattern, and the photometric calibration data had more scatter.

We have also seen evidence for nonlinearity in other data sets with this chip. For example, Figure 4 shows a star-by-star comparison of photometry measured from two images of the same uncrowded field in chip 1. The two images were taken in 1998 December two nights apart. They were processed identically, and photometry was measured in the same manner. They are different in two ways. Frame 2 was

[4] Available at http://tdc-www.harvard.edu/software/catalogs/ua2.html.

[5] At http://adc.gsfc.nasa.gov/.

TABLE 4

ASTROMETRY AND PHOTOMETRY

l[a]	b[b]	R.A.[c]	Decl.[c]	Chip	M	Err	$M-T_2$	Err	$M-51$	Err	$C-M$	Err	$E(B-V)$
3.7039	61.6057	14 31 33.11	11 12 50.2	2	18.253	0.005	1.651	0.012	−0.322	0.009	1.415	0.009	0.028
11.8001	51.8498	15 14 17.64	9 13 44.9	2	17.074	0.005	0.872	0.009	−0.054	0.012	0.628	0.006	0.031
17.1003	46.9512	15 38 30.94	9 38 28.9	2	19.473	0.012	1.666	0.014	−0.307	0.025	1.409	0.028	0.038
217.9004	37.4270	9 14 57.20	12 28 08.6	4	17.353	0.006	1.353	0.011	−0.156	0.008	1.185	0.008	0.027
223.3000	42.9583	9 42 37.42	11 09 29.0	4	18.909	0.010	1.738	0.013	−0.316	0.015	1.488	0.016	0.019

NOTES.—Table 4 is presented in its entirety in the electronic version of the Astronomical Journal. A portion is shown here for guidance regarding its form and content. Units of right ascension are hours, minutes, and seconds, and units of declination are degrees, arcminutes, and arcseconds.

[a] Galactic longitude.

[b] Galactic latitude.

[c] J2000.0 coordinates.

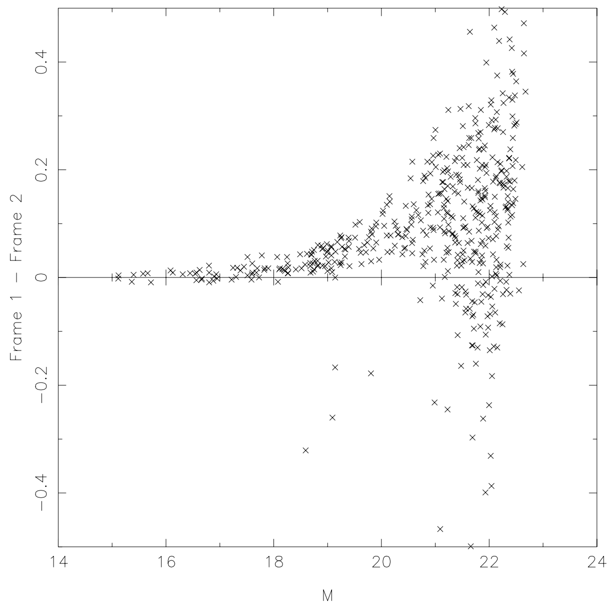

FIG. 4.—Star-by-star comparison of photometry measured from chip 1 (our notation). The data comes from a previous data set taken in 1998 December. The two images were identical except frame 2 has a higher sky level and better seeing conditions. The photometry clearly deviates at faint magnitude, while none of the other three chips show this behavior.

taken when the sky was ∼4 times brighter than for frame 1. Frame 2 was also taken under better seeing conditions. They have the same exposure time. The frame with higher counts (due to the sky) returns brighter values for the faint magnitudes. This behavior is not seen in the other three chips of these same exposures. We believe the difference is due to nonlinear response of the chip.

We have included the stars from chip 1 (traditional chip 2) in the plots and tables because we have successfully found halo giants from candidates on this chip. Also, removing these stars from the plots does not alter the appearance of

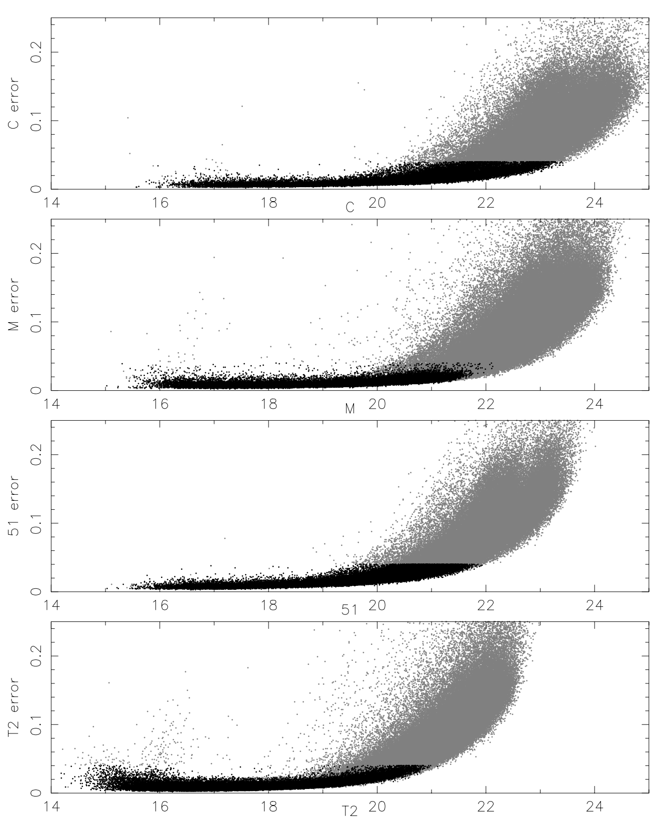

FIG. 5.—Error distribution of stars for all 53 fields. The black points represent stars with errors below the cutoff, 0.04, in all four filters. The gray points represent stars that did not pass this criterion.

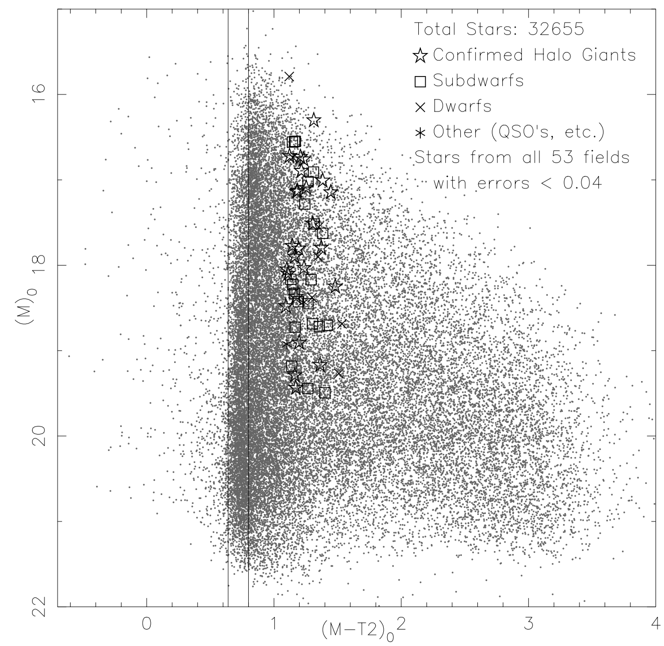

FIG. 6.—Color-magnitude diagram for all 53 fields. This plot only includes stars whose errors lie below 0.04 in all measurements. Extinction corrections have been applied. The two vertical lines indicate the turnoff color indices for the halo ($M - T_2 = 0.64$) and the thick disk ($M - T_2 = 0.8$). The stars marked with special symbols indicate preliminary results from spectroscopic observations. The stars are confirmed halo giants, the squares are metal-poor subdwarfs, the crosses are foreground dwarf stars, and the asterisks are QSOs and other nonstellar objects.

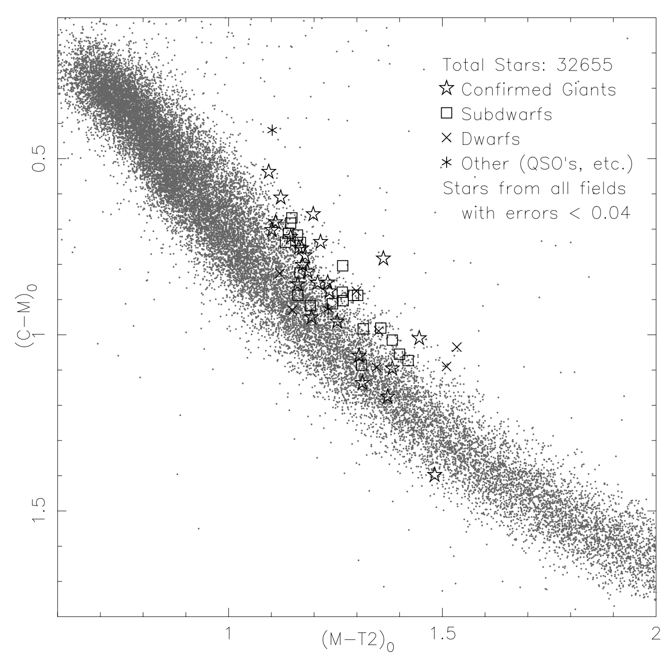

FIG. 7.—Color-color diagram including stars from all 53 fields with errors less than 0.04. Extinction corrections have been applied. Also marked with special symbols are preliminary results from spectroscopic observations, as in Fig. 6.

the plots nor decrease the scatter. However, the chip number is listed in Table 4 so the reader can identify these stars if desired.

The DoPHOT internal error distributions for all stars in all fields is shown in Figure 5. For reference, the average errors for a star at $M = 18.5$ are 0.009, 0.008, 0.011, and 0.009 for C, M, DDO51, and T_2, respectively. Selection for halo candidacy was restricted to stars with internal errors better than 0.04. These stars (Table 4) are shown in black, while stars not selected are shown in gray. The error must have been less than this cutoff in all filters where the star was detected to have been a possible candidate.

The turn-up of stars to higher errors at faint magnitudes is rather broad. This is because we have included stars from all 53 fields. The distribution from an individual field is much narrower. We achieved different depths for each field because of variations in sky brightness and seeing. For example, the photometric depth for an average M error of 0.04 ranges from $M = 20.8$ in field l3263bp386 to $M = 22.3$ in field l2637bp330.

Figure 6 shows the color-magnitude diagram for stars with errors below the cutoff, and for all 53 fields. We have included lines indicating the halo turnoff color index ($M - T_2 = 0.64$) and the thick disk turnoff color index ($M - T_2 = 0.80$) (see Paper I for the determination of these color indices).

The high quality of these data make two populations readily apparent. The thick disk turnoff stars show a concentration with $16 \lesssim M \lesssim 18.5$ just redward of $M - T_2 = 0.80$. The halo turnoff stars are found just redward of $M - T_2 = 0.64$. They are found at all magnitudes, but increase in number toward fainter magnitudes. As discussed in Paper I, stars between these two color indices comprise our halo turnoff candidate stars. Notice that these two populations have sharp cutoffs in color index. This indicates the photometry calibration is extremely accurate, so as not to blur these populations when combining data from different chips and different fields.

Figures 7 and 8 are the color-color diagrams for stars with errors below the cutoff and for all 53 fields. The narrow sequences in these diagrams attest to the high quality of these data, as well as the excellence of the relative calibration between fields. These diagrams are used for identifying halo giant candidates. The details of this selection

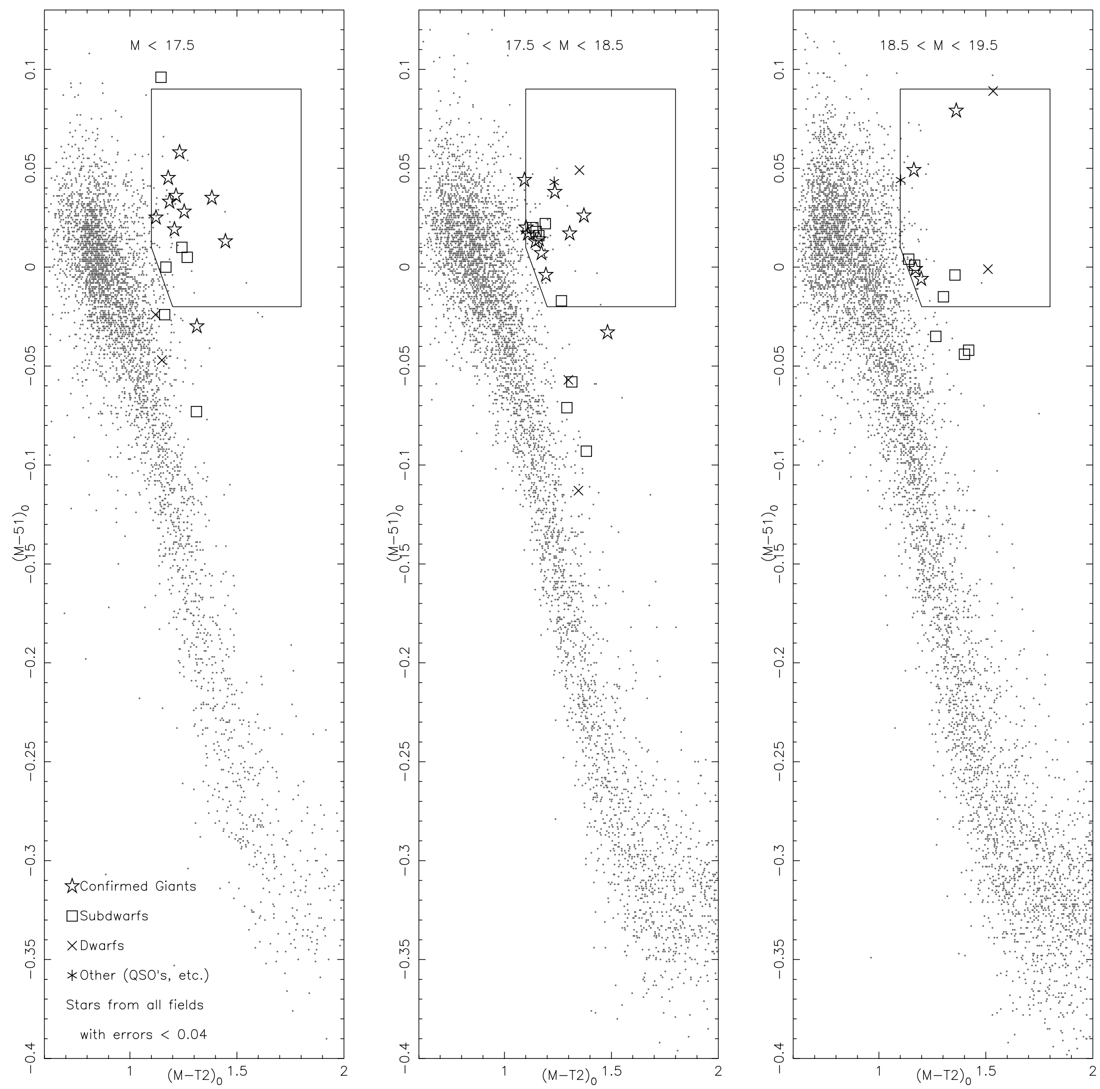

FIG. 8.—Color-color diagram including stars from all 53 fields with errors less than 0.04. Extinction corrections have been applied. The plot has been divided into three magnitude regions, as indicated in the upper right. The bounded region is where we expect to find giant stars. Also marked with special symbols are preliminary results from spectroscopic observations, as in Fig. 6.

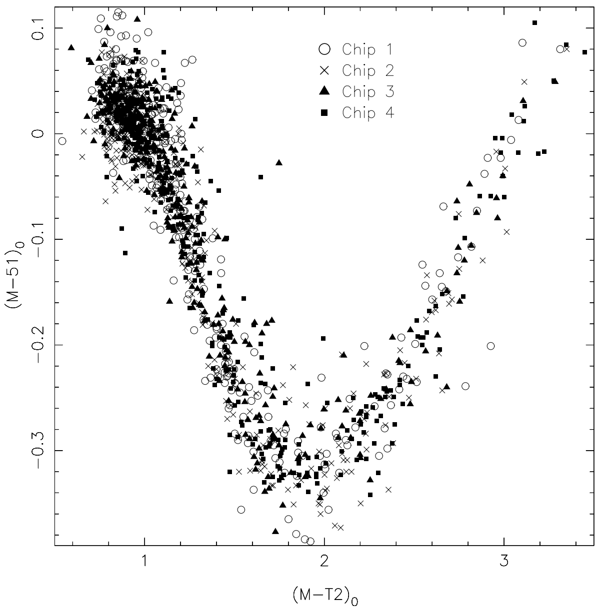

FIG. 9.—Color-color diagram for field l3430bm359. Each of the BTC chips is marked with a different symbol.

process are outlined in Paper I. Below we provide a brief overview of this process to demonstrate our photometric accuracy, and the limitations of photometric selection.

$C-M$ is our primary metallicity indicator. Lower metallicity stars of a given effective temperature will have a bluer $C-M$ value. Halo stars are expected to be lower metallicity than disk and thick disk stars. Hence, they are found on the right side of the stellar sequence in Figure 7. $M-51$ is sensitive to surface gravity. The dwarfs define a clear sequence that dips to low $M-51$ values (Geisler 1984; Paltoglou & Bell 1994). Giant stars, by contrast, are expected to follow a different sequence with $M-51$ values that remain near zero (see Paper I).

We have no overlapping fields to test the relative photometric calibration between fields. However, we can assess the quality from the narrowness of the sequence of stars in the color-color diagrams. For instance, the rms deviation of stars about the locus of points in Figure 7 is approximately 0.07. The scatter for a single field is also approximately 0.07. Hence, the increased scatter due to relative calibration errors is at most 0.02. To provide a visual impression of this quality, we have plotted a color-color diagram for a single field (Fig. 9). Each of the BTC chips is marked with a different symbol. None of the chips shows an obvious offset with respect to the others. Hence, we have judged the relative photometry between chips and between fields to be excellent.

Halo giant candidates are chosen from among those stars that occupy both the low metallicity region in Figure 7 and the giant region of Figure 8. It is evident from Figure 8 that dwarfs far outnumber giants. In fact, there are not enough giants to form a clear sequence.

We have added symbols to Figures 6, 7, and 8 to indicate preliminary results of spectral follow-up on a subset of the giant candidates. The stars indicate stars that have been confirmed to be halo giants, squares indicate metal-poor subdwarfs, crosses indicate dwarfs, and asterisks indicate nonstellar objects. Our selection of candidates was meant to explore the regions of these diagrams and identify the most efficient means of selecting giant candidates.

These figures indicate that giant stars are readily found in the correct locations, but there is some contamination from dwarfs. The dwarf population arises from two sources. First, and most problematic, are low-metallicity subdwarfs. These are photometrically indistinguishable from giants, and we cannot eliminate them using photometric observations alone. Second are normal disk dwarfs whose photometric errors scatter them into the selection region. These can largely be eliminated with high-precision photometry and by using selections based on both luminosity $(M-51)$ and metallicity $(C-M)$.

As expected, this contamination is worse for fainter stars. Figure 8 is divided into three magnitude bins to demonstrate this effect. The confirmed giants occupy a fairly well bounded region defined by $-0.02 \lesssim (M-51) \lesssim 0.09$, and $1.1 \lesssim (M-T_2) \lesssim 1.8$. This region is marked in Figure 8. Note that we have observed some stars spectroscopically outside this region in order to explore the diagram and optimize future candidate selection. In fact, it was this exploration that helped define this region. The candidates with $(M-51) \lesssim -0.02$ turn out to be predominately dwarfs. The giants not within this bounding box have a fairly high metallicity ([Fe/H] ~ -0.6) and would not normally pass the $C-M$ criteria (see Fig. 7).

The number of observed candidates within the bounding box defined above is 40. Of these, 22 are confirmed giants for a global identification efficiency of 55%. However, this efficiency is a strong function of magnitude, and the overall giant selection efficiencies are 75%, 59%, and 36% for $M < 17.5$, $17.5 < M < 18.5$, and $18.5 < M < 19.5$, respectively.

It is more instructive to break these numbers up by subdwarf versus dwarf. The only true failures of the photometric selection are the dwarfs, which scatter into the giant region by measurement errors. The subdwarfs and nonstellar objects will always be found within this region and cannot be separated from giants by photometry alone. If we restrict the failure count to only dwarfs, the efficiencies, as a function of magnitude, are 100%, 94%, and 82% for $M < 17.5$, $17.5 < M < 18.5$, and $18.5 < M < 19.5$, respectively. These are very high efficiencies due to the excellent quality of the photometry.

The ratios of giant to subdwarf are 3, 2, and 1 for $M < 17.5$, $17.5 < M < 18.5$, and $18.5 < M < 19.5$, respectively. This makes going after faint, distant giants difficult. However, we have learned much from these first observations, and by adjusting our selection criteria we can eliminate many of these subdwarfs. For example, by increasing the lower bound of the selection region (Fig. 8), most of the subdwarfs are eliminated, at the expense of missing several giants. At this point it is unclear where the optimal bounds are to maximize the number of giants. Employing such modifications, we expect our future efficiency to be even higher. Morrison et al. (2000b) explores how this efficiency is affected by photometric precision and how to further optimize halo candidate selection.

5. SUMMARY

We are conducting an imaging survey of high Galactic latitude fields to examine the structure of the Galactic halo. Thus far we have observed 134 separate fields covering a total area of 52 deg². We have used three different telescopes, and four different instruments. We present the details of our automated pipeline reductions designed to handle this large volume of data.

We present results from our most successful observing run using the BTC camera on the CTIO 4 m in 1999 April. These data are available in the electronic version of this paper, as well as through ADC.[5] All other observing runs occurred in partially bad weather and are thus not fully calibrated. These data will be published and made available on-line in the future as calibrating observations are obtained.

We discuss preliminary results in identifying halo giants using the Washington filter set. We achieve an overall giant identification efficiency of 66% for $M < 18.5$. However, most of the nongiant candidates are low-metallicity subdwarfs, which cannot be distinguished from giants using photometric selection alone. The contamination by dwarfs that scatter into the selection region due to photometric errors is only 3% for $M < 18.5$. This high efficiency is only possible with very accurate photometry. We have also learned much from these first observations, and we expect to improve the efficiency through refinements in the selection technique. Details of our efficiency and refinements in the selection process will appear in a future paper (Morrison et al. 2000b).

We would like to thank Doug Geisler, whose efforts with the Washington filter set have made this work possible. This work was supported by NSF grants AST 96-19490 to H. L. M., AST 95-28367, AST 96-19632, and AST 98-20608 to M. M., and AST 96-19524 to E. W. O.

REFERENCES

Arnold, R., & Gilmore, G. 1992, MNRAS, 257, 225
Bailyn, C. D. 1995, ARA&A, 33, 133
Canterna, R. 1976, AJ, 81, 228
Côté, P., Welch, D. L., Fischer, P., & Irwin, M. J. 1993, ApJ, 406, L59
Dixon, R. S. 1981, Transparent Plastic Overlay Map of the Palomar Sky Survey Photographs, Bull. d'Inf. Cent. Donnees Stellaires, 21, 50
Eggen, O. J., Lynden-Bell, D., & Sandage, A. R. 1962, ApJ, 136, 748
Geisler, D. 1984, PASP, 96, 723
———. 1990, PASP, 102, 344
———. 1996, AJ, 111, 480
Harris, H.C., & Canterna, R. 1979, AJ, 84, 1750
Helmi, A., White, S. D. M., de Zeeuw, P. T., & Zhao, H. 1999, Nature, 402, 53
Ibata, R. A., Gilmore, G., & Irwin, M. J. 1994, Nature, 370, 194
Kinman. T. D., Suntzeff, N. B., & Kraft, R. P. 1994, AJ, 108, 1722
Majewski, S. R. 1992, ApJS, 78, 87
Morrison, H. L., Mateo, M., Olszewski, E. W., Harding, P., Dohm-Palmer, R. C., Freeman, K. C., Norris, J. E., & Morita, M. 2000a, AJ, 119, 2254 (Paper I)
Morrison, H. L., Mateo, M., Olszewski, E. W., Harding, P., Dohm-Palmer, R. C., Freeman, K. C., & Norris, J. E. 2000b, AJ, in press
Norris, J. E., & Hawkins, M. R. S. 1991, ApJ, 380, 104
Paltoglou, G., & Bell, R. A. 1994, MNRAS, 268, 793
Preston, G. W., Beers, T. C., & Shectman, S. A. 1994, AJ, 108, 538
Schechter, P.L., Mateo, M.L., & Saha, A. 1993, PASP, 105, 1342
Schlegel, D. J., Finkbeiner, D. P., & Davis, M. 1998, ApJ, 500, 525
Searle, L., & Zinn, R. 1978, ApJ, 225, 357
Steinmetz, M., & Mueller, E. 1994, A&A, 281, L97
Yanny, B., et al. 2000, ApJ, 540, 825